Electrochimica Acta 470 (2023) 143308

Contents lists available at ScienceDirect

Electrochimica Acta

journal homepage: www.journals.elsevier.com/electrochimica-acta

Exfoliated Graphene Oxide @ Sb_2O_3 Octahedrons as Alloy-Conversion Anode for High-Performance Na-Ion Batteries with P2-Type $Na_{2/3}Ni_{1/3}Mn_{2/3}O_2$ Cathode

Krishnan Subramanyan [a], Murukabhavan Ramar Palmurukan [a], Yun-Sung Lee [b,*], Vanchiappan Aravindan [a,*]

[a] Department of Chemistry, Indian Institute of Science Education and Research (IISER) Tirupati 517507, India
[b] School of Chemical Engineering, Chonnam National University, Gwang-ju, 61186, Republic of Korea

ARTICLE INFO

Keywords:
exfoliated graphene oxide@Sb_2O_3
alloying-conversion
anode
Na-ion battery
$Na_{2/3}Ni_{1/3}Mn_{2/3}O_2$ Cathode

ABSTRACT

Conversion–alloying–based anodes for sodium–ion batteries (SIBs) have attracted wide interest due to their high energy density and specific capacity. However, it suffers from volume expansion during operation, leading to poor cycling stability. This study introduces a novel carbon matrix, exfoliated graphene oxide (EGO), to alleviate the issues due to volume expansion in the antimony (III) oxide anode for SIBs. Four combinations of Sb_2O_3 with EGO were explored, and electrochemical performance was compared. An optimized combination (Sb–E1) showed a capacity of ~100 mAh g^{-1} at a high current density of 1 A g^{-1} with good cycling stability. The results show that EGO can effectively buffer the volume expansion and promote fast kinetics. An *in–situ* electrochemical impedance spectroscopy study revealed that the exceptional charge-transfer resistance varies during the alloying reaction but not during the conversion reaction. The full-cell is fabricated with P2-type layered $Na_{2/3}Ni_{1/3}Mn_{2/3}O_2$ (NNMO) cathode. The Sb–E1/NNMO cell displayed an average operating potential of ~2.95 V, a high capacity of ~100 mAh g^{-1} at a current density of 1 A g^{-1}, and a maximum energy density of ~100 Wh kg^{-1}.

1. Introduction

The constant endeavour to commercialize safe, efficient, mobile, and cheap electrochemical energy storage has opened doors to post lithium–ion battery (LIB) technologies, where sodium–ion batteries (SIBs) are a noteworthy candidate [1–5]. There is ceaseless research on SIBs aiming to improve the operating voltage, energy, and power density. To improve the performance of SIBs, multifarious anodes have been developed, which store Na^+ through intercalation, conversion, and alloying mechanisms or their combinations [6–13]. While the intercalation mechanism offers better cycling stability, it lacks specific capacity, eventually reducing the battery's overall energy density. On the other hand, alloying and conversion–based anodes have significantly higher theoretical capacity [14–16]. However, using alloying and conversion–based anodes is accompanied by some major challenges. a) During cycling, they experience massive volume expansion, eventually leading to particle agglomeration. The volume expansion causes a loss in contact between the current collector and active material. b) Thick solid electrolyte interface (SEI) on the electrodes that increase charge transfer resistance. Such predicaments eventually lead to poor cycling stability [17]. Elements such as Sn, Sb, Bi, Ge, and Si are well known for their alloying reaction with sodium, while oxides, sulfides, selenides, and phosphides of transition metals such Cu, Co, Fe, and Ni can undergo conversion reactions with sodium [18–23]. Antimony (Sb) is a highly–explored alloying material with a theoretical capacity of 668 mAh g^{-1} and a reaction potential of 0.2–0.4 V *vs.* Na. Antimony oxides and antimony–based intermetallic alloys (Sn–Sb, Sb–Si, Sb–Bi) are highly popular for Na^+ storage through the conversion–alloying mechanism [24–27]. Several mechanisms have been proposed to mitigate the volume expansion (~290% for Sb) and its repercussions during cycling. These include constraining the nanosized active material in a carbon matrix and hollow structures to contain the active material core–shell structures [28,29]. Additionally, antimony (III, IV) oxides have poor conductivity and carbon matrices are used to improve it [30].

This study aims to eliminate the volume expansion and its aftermath by incorporating Sb_2O_3 in a chemically exfoliated graphene oxide (EGO) carbon matrix synthesized through a scalable and simple process. The concept of using graphene oxide as a carbon matrix for anchoring

* Corresponding authors.
E-mail addresses: leeys@chonnam.ac.kr (Y.-S. Lee), aravind_van@yahoo.com (V. Aravindan).

https://doi.org/10.1016/j.electacta.2023.143308
Received 31 March 2023; Received in revised form 5 October 2023; Accepted 5 October 2023
Available online 6 October 2023

antimony and oxides has been explored previously [24–29]. We used EGO as a volume buffer for antimony (III) oxides, a novel concept in SIBs for reversible Na^+ storage. EGO has been explored in heterogenous catalysis as a stable substrate for the metal nanocatalyst [31]. This carbon support is extremely stable, and the catalyst could be successfully recycled after the reaction. This was the motivation for exploring exfoliated graphene oxide as the support for antimony (III) oxide. We explored different ratios of antimony to carbon by tuning the mass of the antimony precursor to the carbon matrix before pyrolysis. We have explored four such combinations of Sb_2O_3:EGO – 750:140, 750:70, 750:46.6, and 750:23.3, which are referred to in the manuscript as Sb–E1, Sb–E2, Sb–E3, and Sb–E4, respectively. These compositions were tested in sodium–ion half–cells to optimize the cycling stability and rate performance. The composition exhibiting optimum performance has been assembled into a balanced sodium–ion full–cell with P2 type layered–$Na_{2/3}Ni_{1/3}Mn_{2/3}O_2$ cathode.

2. Experimental section

2.1. Synthesis of Sb_2O_3–EGO

Exfoliated graphene oxide (EGO) was synthesized through a reported procedure [31] where commercially available graphite powder (was used as the precursor. Sb–EGO's compositions have been synthesized through the same procedure. $C_6H_9O_6Sb$ (>99.99%, Sigma Aldrich) and ethanol (>99.9 %) have been used without any purification. $C_6H_9O_6Sb$ and EGO were dispersed in 25 mL and 75 mL of ethanol in individual beakers through probe sonication. Subsequently, they were mixed and again sonicated. During probe sonication, the beakers were kept in an ice bath to avoid an increase in temperature. The probe was immersed in the solution, leaving a small gap between the beaker's base and the probe. The probe sonication involved ten cycles, with 60% amplitude for the first five and 80% amplitude for the next five. Each cycle consisted of one minute pulse ON followed by 30s rest. The mixture was transferred into a round bottom flask and subjected to forced vacuum drying until the solvent was completely removed. This was kept in a 65 °C oven until the above powder was completely dried. The precursor was then transferred into a ceramic crucible and heated at 400 °C for 4 hours in an argon atmosphere, with a heating ramp rate of 5 °C/min. After natural cooling to room temperature, the product, Sb_2O_3–EGO, was ground with a mortar pestle and used for electrochemical studies.

The product's Sb_2O_3 to EGO ratio was controlled by fixing the mass of $C_6H_9O_6Sb$ and adjusting the mass of EGO. 2.5 mmol of $C_6H_9O_6Sb$ was used with 140, 70, 46.6, and 23.3 mg of EGO to obtain Sb–E1, Sb–E2, Sb–E3, and Sb–E4, respectively. The synthesis of Sb_2O_3–EGO is summarized in Scheme 1.

2.2. Synthesis of P2–type $Na_{2/3}Ni_{1/3}Mn_{2/3}O_2$ (NNMO)

NNMO was synthesized through sol–gel method as shown in **Scheme S1**, according to previous report [40]. A homogenous solution of sodium nitrate ($NaNO_3$, >99%, Sigma Aldrich), nickel nitrate hexahydrate ($Ni(NO_3)_2.6H_2O$, 99%, Loba Chemie), manganese nitrate tetrahydrate ($Mn(NO_3)_2.4H_2O$, 97%, Sigma Aldrich) in 2.08:1:2 molar ratio was dissolved in deionized water and stirred for 30 minutes in room temperature. This solution was added dropwise to 20 mL of ethylene glycol (99.8%, anhydrous, Sigma Aldrich) under continuous vigorous stirring, and the obtained mixture was heated at 80 °C to obtain the gel precursor. This precursor was heated in a muffle furnace at 850 °C for 3 hours with a ramp rate of 3 °C/min and was allowed to cool naturally to room temperature to obtain the final product.

2.3. Material characterization

X–ray diffraction studies of all the samples were performed in Rigaku Smartlab automated multipurpose X–ray diffractometer with a monochromatic Cu Kα radiation (λ = 1.5604 Å). X–ray photoelectron spectroscopy (XPS, Multilab, 2000, UK) was performed to study the surface chemistry of the materials. The surface imaging of the samples was studied through scanning electron microscopy (FE–SEM S–4700, Hitachi, Japan), and high–resolution transmission electron microscopy (HR–TEM, JEM–2000, EX–II, JEOL, Japan) was used to study the crystal structure and morphology. The carbon content in Sb–E1 was estimated through thermogravimetric analysis (TGA, Shimadzu, Japan), with a 5 °C min^{-1} ramp rate in the air atmosphere. LabRam HR800 UV Raman microscope (Horiba Jobin– Yvon, France) with a 515 nm diode laser as a light source was used to record the Raman spectra of Sb–E1 at room temperature.

3. Electrochemical characterization

3.1. Electrode fabrication

All the Sb_2O_3–EGO samples were coated on copper foil with an active material: conductive carbon: binder ratio of 70:10:20 wt.%. To begin with, the binder, polyvinylidene fluoride binder (PVDF), is dissolved in 1–methyl–2–pyrrolidinone (NMP, anhydrous, Sigma Aldrich, >99.5%). Following this, the conductive additive (acetylene black, AB) and active material (Sb_2O_3–EGO) were added to the above and stirred at room temperature overnight. The homogenous slurry thus formed was coated onto copper foil using the doctor blade technique and dried at 65 °C in an air oven. Subsequently, a calendar press was used to press the copper foil, and 12 mm electrodes were punched.

NNMO electrodes for half–cell testing were made following the above method, but the ratio of NNMO: AB: PVDF was 70:20:10 wt.%. NNMO electrodes for full–cell testing were fabricated on 14 mm SS mesh (Goodfellow, UK) current collector. For this, a free–standing film was prepared in a mortar pestle with active material (NNMO), conductive carbon (AB), and teflonized acetylene black (TAB-2, binder) with ethanol as a solvent and was pressed onto the SS mesh using Specac hydraulic press. The ratio of NNMO:AB:TAB was adjusted to 70:15:15 wt.%. The mass of NNMO for the full–cell was adjusted according to the mass and capacity of the Sb–E1 after pre–cycling to construct a balanced full–cell. Mass balancing was performed according to the formula.

$$m_{anode} \times C_{anode} = m_{cathode} \times C_{cathode}$$

m is the mass of active material, and C is the specific capacity.

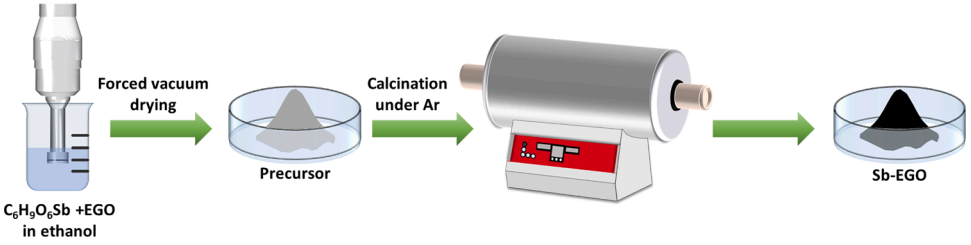

Scheme 1. Synthesis of Sb–EGO.

3.2. Half and full–cell studies

All the cells were assembled inside an MBraun inert glove box workstation with O_2 <0.1 ppm and H_2O <0.1 ppm in a CR2016 coin–cell. A glass microfiber separator was used in all the cells (Whatmann, cat no. 1825–047, UK). The electrolyte used was 1M sodium perchlorate ($NaClO_4$, Sigma Aldrich, >98%) dissolved in 1.1 vol.% of propylene carbonate (PC, anhydrous, Sigma Aldrich, >99.7%) and dimethyl carbonate (DMC, anhydrous, Sigma Aldrich, >99%) with 5 vol.% of fluoroethylene carbonate (FEC, Sigma Aldrich, >99%) additive. The half–cells were assembled with sodium metal foil as a reference and counter electrode. Before cell assembly, all the electrodes were kept in a vacuum oven for 4 hours at 75 °C to ensure complete drying. Sb–E1 electrodes were cycled four times before assembling into full–cells. These pre–cycled coin–cells were opened, and the electrode was carefully removed from the cell and assembled with an NNMO cathode to make the full–cell. BioLogic battery tester (BCS–805) was used to perform all the electrochemical tests. The specific capacity of half and full–cells have been calculated by taking the anode active material mass. The specific energy and power density have been calculated with the anode's and cathode's active material mass.

4. Results and Discussion

The material characterization of Sb–E1 is shown in Fig. 1. The major sharp peak in the X–ray diffraction (XRD) at 2θ=22.66° (Fig. 1**(a)**) corresponds to the (222) plane of Sb_2O_3 crystal. All the peaks can be indexed to Sb_2O_3 (DB card # 01–071–0365). The XRD pattern does not show the presence of any impurity in the sample. The peaks are sharp and well–distinguished, indicating the highly crystalline nature of Sb–E1. No broad peaks correspond to the carbon matrix, which points to the high antimony loading in the material. For comparison, the XRD patterns of Sb–E2, Sb–E3, Sb–E4, and EGO are shown in **Fig. S1**. The XRD patterns of the antimony–EGO samples are similar, ensuring the presence of highly crystalline Sb_2O_3 in all the samples. The broad peak seen in the XRD analysis of EGO, representing the amorphous carbon, is absent in all the antimony samples, indicating a high antimony–to–carbon weight ratio. The Raman spectra of Sb–E1, shown in Fig. 1**(b)**, have peaks corresponding to Sb_2O_3 and EGO. The sharp peaks at 256, 358, 378, 455, and 711 cm^{-1} correspond to cubic Sb_2O_3. The Raman peak observed at 455 cm^{-1} belongs to Sb–O–Sb bending mode, whereas the peaks at 256, 358, 378, and 711 cm^{-1} are from the Sb–O–Sb stretching modes. These are in agreement with the reported literature [32]. Two broad peaks at 1350 and 1580 cm^{-1} are the D and G band peaks arising from EGO (inset of Fig. 1**(b)**). The I_D/I_G ratio is calculated to be ~1, which denotes the disordered structure of EGO. **Fig. S2** shows the X–ray photoelectron spectra (XPS) of Sb–E1, where multiple peaks can be indexed to Sb 3d, Sb 3p, O 1s, and C 1s. Fig. 1**(c)** and **1(d)** show the deconvoluted XPS peaks. The peaks in Fig. 1**(c)** at 530.1 and 539.5 eV binding energies correspond to Sb $3d_{5/2}$ and Sb $3d_{3/2}$, indicating the presence of antimony (III) oxide in Sb–E1. There are two deconvoluted peaks belonging to O 1s, which are marked in Fig. 1**(c)**. The C 1s peak (Fig. 1**(d)**) can be deconvoluted into three peaks at 284.6, 286.4, and 289 eV. These peaks arise from graphitic carbon (C–C sp^2), C–O, and O–C=O present in EGO [33–35]. A quantitative estimation of carbon content in Sb–E1 is obtained from thermogravimetric analysis (TGA, **Fig. S3**), which showed ~27 wt.%.

The Sb–E1 was analyzed using scanning electron microscopy (SEM) and transmission electron microscopy (TEM) studies. The imaging techniques reveal that Sb_2O_3 has been homogenously distributed in the carbon matrix. The broken graphene oxide (GO) sheets embedded with Sb_2O_3 particles are clearly visible in the SEM image in Fig. 1**(e)**. The Sb_2O_3 particle sizes range from a few nanometers to a few hundred nanometers with irregular morphology. The absence of agglomeration among Sb_2O_3 particles and homogenous distribution in the carbon matrix is attributable to probe sonication during the synthesis. Well–distinct (222) crystal planes separated by 0.32 nm can be seen in a higher–resolution TEM image of the Sb_2O_3 particles (Fig. 1**(h)**). The selected area electron diffraction (SAED) pattern in Fig. 1**(i)** shows the polycrystalline nature of the material, of which two rings can be indexed to (222) and (111) planes [36]. The presence of Sb, O, and C is further confirmed through elemental mapping (Fig. 1**(j–m)**).

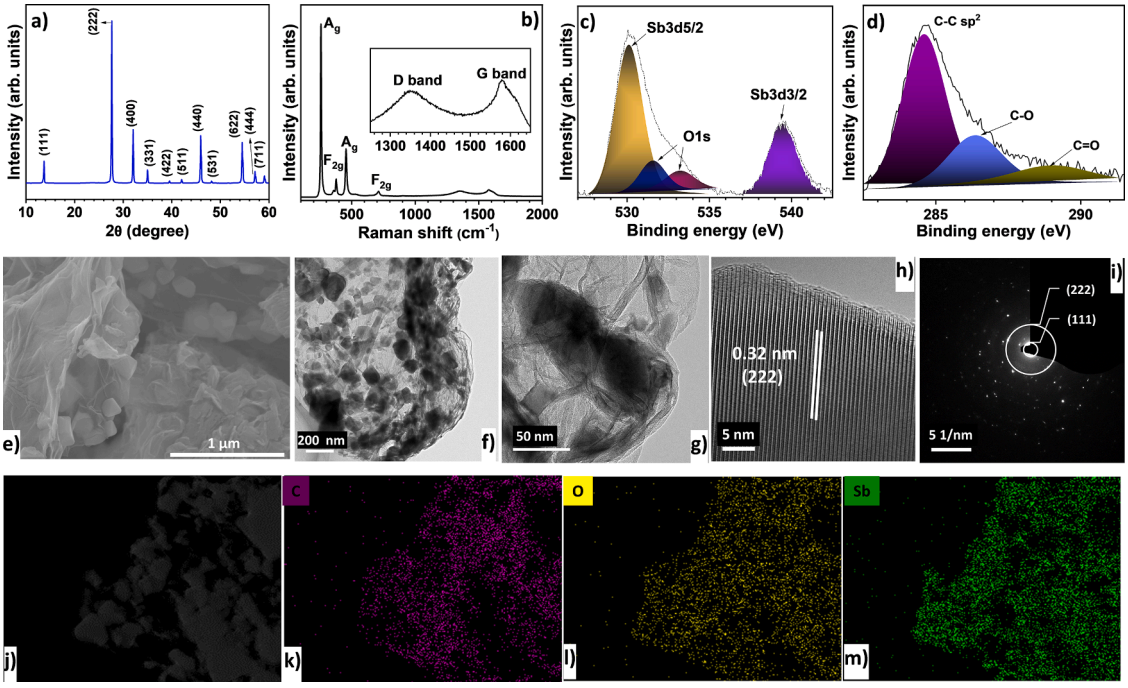

Fig. 1. (a). XRD pattern of Sb–E1, **(b)** Raman spectra of Sb–E1; peaks arising from D and G band of carbon are given in the inset, deconvoluted XPS peaks of **(c)** Sb3d and O1s, and **(d)** C1s, **(e)** SEM image of Sb–E1, **(f–h)** TEM images of Sb–E1, **(i)** SAED pattern for Sb–E1, and, **(i)** Bright-field TEM image of Sb–E1, elemental mapping of **(k)** C, **(l)** O, and, **(m)** Sb.

First, the Sb–E1, Sb–E2, Sb–E3, and Sb–E4 samples were subjected to half–cell studies. Sb_2O_3 undergoes a conversion–alloying reaction during Na^+ storage. This reaction can be represented as[28,37]:

$$1^{st}\text{discharge}: \quad Sb_2O_3 + xNa^+ + xe^- \rightarrow xSb^0 + xNa_xSb_2O_3$$
$$xNa_xSb_2O_3 + (6-x)\,Na^+ + (6-x)e^- \rightarrow 2Sb^0 + 3\,Na_2O$$
$$Sb^0 + xNa^+ + xe^- \rightarrow Na_xSb$$

Subsequent cycles:

$$(\text{Conversion reaction}) \quad Sb_2O_{3_{amorphous}} + 6Na^+ + 6e^- \leftrightarrow 2Sb^0 + 3Na_2O$$

$$(\text{Alloying reaction}) \quad Sb^0 + xNa^+ + xe^- \leftrightarrow Na_xSb$$

Fig. S4 is the first cyclic voltammetry curve for all Sb–E samples. The major reduction peaks for all the samples are at ~0.005 and ~0.38 V *vs.* Na. The large cathodic peak at 0.38 V *vs.* Na arises from the structural reorientation and the electrolyte decomposition at the electrode surface, forming a SEI, in addition to the conversion reaction and subsequent formation of Na_xSb [38]. The peak at 0.005 V *vs.* Na can also be ascribed to the alloying reaction, leading to the formation of the Na_xSb phase. A minor reduction peak around 1 V *vs.* Na is seen in all the samples, and this peak current increases with increasing EGO content. According to previous reports [38], such a peak is absent in the first cycle for pure Sb_2O_3. Hence this might be arising from the electrochemical reactions with EGO since the increasing peak current can be correlated with increasing EGO content in the sample. The oxidation peaks in the reverse scan during the first cycle are at ~0.8 V *vs.* Na, and the broad peak is at ~1.50 V *vs.* Na. These peaks do not change in the subsequent cycle and represent the dealloying and formation (conversion of Sb^0 into its oxide) of Sb_2O_3, respectively [39] (Fig. 2**(a)**). There are major changes in peak current, along with the appearance of new peaks in the cathodic scan in the second cycle (Fig. 2**(a)**). The additional peak at 0.90 – 1 V *vs.* Na for all the samples can be assigned to the conversion reaction, leading to the formation of Sb^0. All the other anodic peaks (0.38 and 0.005 V *vs.* Na) can be assigned to the alloying reaction. The peak current at 0.38 V *vs.* Na drastically decreases compared to the first cycle, affirming that the additional current contribution is due to the irreversible Na^+ consumption.

The electrochemical performance of bare EGO and commercially purchased Sb_2O_3 was evaluated in half–cell configuration in the voltage window 0.005 – 3.00 V *vs.* Na (**Fig. S5 and S6**). EGO's galvanostatic charge–discharge (GCD) curves portray typical pseudocapacitive adsorption–based Na^+ storage. Within 50 cycles, the specific capacity falls below 50% of its initial capacity. Commercially obtained Sb_2O_3 half–cell shows a very poor performance, where the specific capacity drops to an inappreciable value within ten cycles. The electrochemical performances of Sb–EGO samples were compared by studying their rate performance and long–term cycling. Sb–E1 displays the best rate performance with the highest capacity value of ~113 mAh g^{-1} at a current density of 1000 mA g^{-1}, shown in Fig. 2**(b)**. The rate performance of Sb–E (2–4) and their GCD curves is given in **Fig. S7**. Before rate performance, the cells were subjected to 7 cycles of GCD at a current density of 25 mA g^{-1}. The capacity at the current density of 1000 mA g^{-1} is strongly influenced by the ratio of Sb_2O_3 to EGO. Sb–E1, with the highest EGO content, offered the highest capacity at current density of 1000 mA g^{-1}, followed by Sb–E2, Sb–E3, and Sb–E4 in that order. Fig. 2 **(e)** shows the cycling test of all the samples for 100 cycles at current density of 100 mA g^{-1} from 0.005 to 3.00 V *vs.* Na. The average operating potential of the cell is determined to be 0.77 V *vs.* Na at a current density of 100 mA g^{-1}. The initial irreversibility is highest for Sb–E1 due to the highest carbon content. The specific discharge capacity in the second cycle is 545, 320, 325, and 353 mAh g^{-1} for Sb–E1, E2, E3, and E4, respectively. After 100 cycles, the capacity of Sb–E1 is 345 mAh g^{-1},

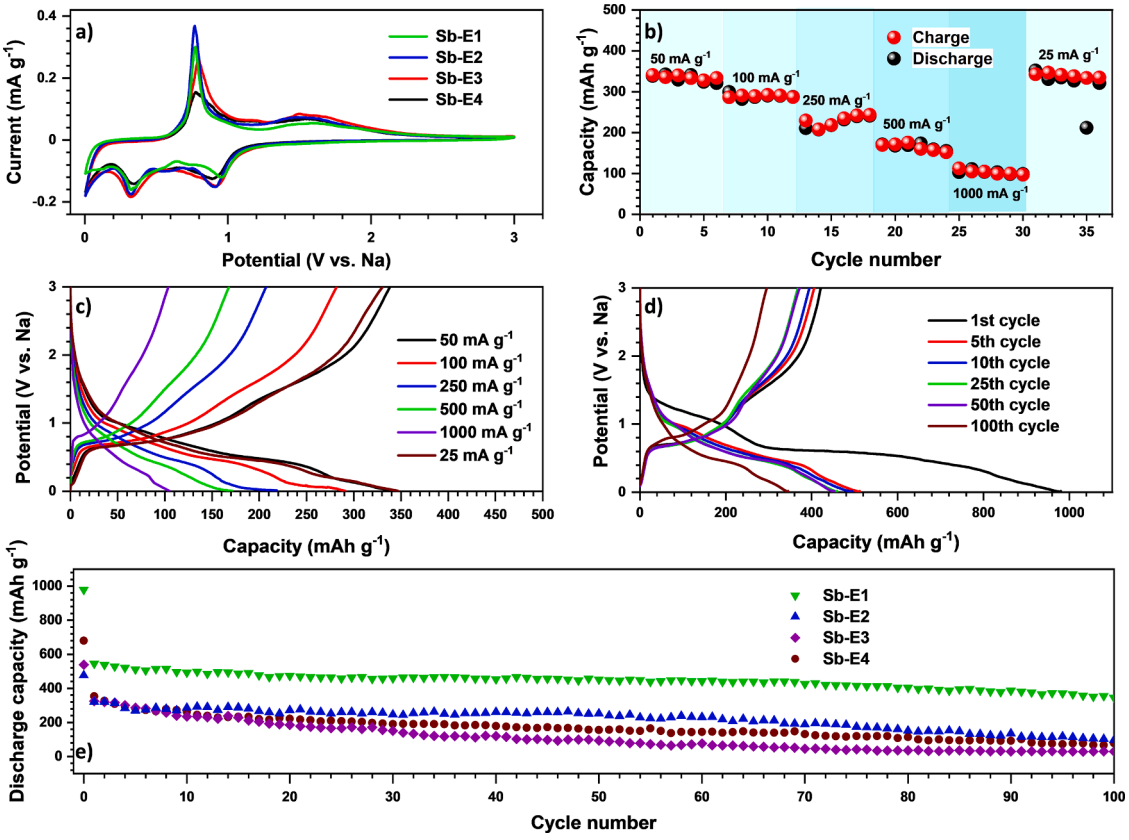

Fig. 2. **(a)** CV curves of Sb–E1, Sb–E2, Sb–E3, and Sb–E4 at a scan rate of 0.1 mV s^{-1}, **(b)** specific capacity during rate performance of Sb–E1 half–cell at current density of 50,100, 250, 500, 1000, and 25 mA g^{-1}, **(c)** GCD curves of Sb–E1 half–cell during rate performance, **(d)** GCD curves of Sb–E1 half–cell during long term cycling, and **(e)** long term cycling performance of Sb–E1, Sb–E2, Sb–E3, and Sb–E4 half–cells. All the half–cell testing has been done from 0.005 to 3.00 V *vs.* Na.

which is a capacity retention of 66% with respect to the first reversible capacity. Sb–E1 displays the highest capacity and capacity retention for long–term cycling, owing to the higher EGO content. The GCD curves of Sb–E1 for rate performance and long–term cycling is shown in Fig. 2**(c, d)**. For comparison, the GCD curves of Sb (E2–E4) are shown in **Fig. S8**. It can be seen that after a high current rate, when tested at a current density of 25 mA g^{-1}, Sb–E1 half–cell retains the shape of the GCD curve prior to the high current testing, showing the robustness of the material. Though capacity decay is noticeable in all these samples, the decay rate is gradual (Sb–E2< Sb–E3< Sb–E4), in the order of decreasing EGO content. The plateaus in the GCD curve match exactly with the peaks in the CV curve. The first discharge in the long–term cycling has a capacity much higher than the second cycle, indicating irreversible reactions, which was also seen in the CV curves. EGO abets high current performance and GCD cycling test through three factors: (a) It is flexible support that cushions the volume expansion of Sb_2O_3 during charging and discharging, (b) EGO boosts the electronic conductivity, promoting fast kinetics, and (c) The optimum loading of EGO averts agglomeration of Sb_2O_3.

An *in-situ* electrochemical impedance study (*in-situ* EIS) of the Sb-E1 half–cell was conducted over 50 cycles to examine changes in charge-transfer resistance. EIS covered a frequency range from 10 kHz to 1 Hz with a 10 mV voltage amplitude. A detailed Nyquist plot in Fig. 3 illustrates each potential during discharge and charge, focusing on the high-frequency region. **Fig. S9** presents the charge-transfer resistance (R_{CT}) *vs.* cycle number during charge and discharge. R_{CT} increases during discharge cycles (except for the first cycle), with the highest value occurring at a cell voltage of 0.005 V *vs.* Na. The notable increase in R_{CT} at the end of discharge could be attributed to two scenarios.

Firstly, the possibility of the destruction and reformation of the SEI layer was considered. The initial R_{CT} at 2 V *vs.* Na before the first discharge exceeded 450 Ω but decreased to around 110 Ω after the first charge. In subsequent cycles, the R_{CT} remained below 80 Ω at the charged state. However, at the end of each discharge, R_{CT} increased, although not as dramatically as after the initial discharge. Importantly, CV curves did not display peaks corresponding to electrolyte decomposition, suggesting that SEI destruction and reformation were unlikely.

Alternatively, increased R_{CT} values during discharge, particularly at 0.40 V *vs.* Na, may be attributed to an alloying reaction between Na^+ and Sb^0. Further confirmation of this scenario could be achieved by analyzing EIS curves during the charging process. EIS measurements during charging were recorded at cell voltages ranging from 0.1 to 3 V *vs.* Na. The highest R_{CT} values occurred for EIS curves up to 0.75 V *vs.* Na during charging, after which they began to decrease. Notably, a CV peak centered at 0.8 V *vs.* Na represented the desodiation reaction. Consequently, the second scenario explains the elevated R_{CT} values at low cell voltages more plausibly.

A full–cell study with Sb–E1 anode and $Na_{2/3}Ni_{1/3}Mn_{2/3}O_2$ (NNMO) cathode was conducted in the potential limit of 3.7–1.7 V *vs.* Na. NNMO was synthesized *via* sol–gel route as shown in **Scheme S1**. The as–synthesized NNMO was subjected to material characterization techniques such as XRD, XPS (**Fig. S10**), SEM, and TEM (**Fig S11 (a–d).**). In the XRD (**Fig. S10(a)**), a well–defined sharp peak is seen at $2\theta = 15.9°$, which corresponds to the (002) plane. The XRD spectra convey a highly crystalline nature of NNMO. XPS survey spectrum (**Fig. S10(b–e)**) reveals the presence of multiple peaks, which have been deconvoluted and indexed to Na, Ni, Mn, and O, which is affirmed through the elemental analysis (**Fig. S11(e–f)**). All the above results are in good agreement with the reported literature [40]. NNMO has a plate–like structure, forming agglomerates (**Fig. S11(a,c)**). The SAED pattern confirms the highly crystalline nature of NNMO.

The electrochemical studies of NNMO (CV, rate performance, long–term cycling) were carried out in half–cells in the potential range of 2–4 V *vs.* Na and shown in **Fig. S12**. The cathode shows highly commendable rate performance and an average operating potential of ~3.4 V *vs.* Na, making it an ideal candidate to be paired with Sb–E1. Long–term cycling shows a minimal capacity loss (~0.1%) after 100 cycles at current density of 100 mA g^{-1}. After running CV tests, the full cell potential limit was set as 1.7–3.7 V. The anode was pre–cycled prior to full–cell assembly. Fig. 4**(a)** is the CV for the Sb–E1/NNMO at a scan rate of 0.1 mV s^{-1}. During charge, the CV curves exhibited a sharp peak at 2.94 V and two broad peaks at 2.65 and 1.96 V. While discharging, a sharp peak can be seen at 3.20 V and a broad shoulder peak at 2.95 V. Sb–E1/NNMO has promising rate performance results (Fig. 4**(b)**), where capacity is 101 mAh g^{-1} at a current rate of 1000 mA g^{-1}. The full–cell is not devoid of initial irreversibility during the first charge, even after pre–cycling of the anode, during the long–term cycling at current density of 200 mA g^{-1}, shown in Fig. 4**(c)**. This might arise from the irreversibility in the cathode. The initial discharge capacity is 226 mAh g^{-1}; after 100 cycles, it reaches 116 mAh g^{-1} with 51% of the initial capacity retention.

The Ragone plot of the Sb–E1/NNMO is shown in Fig. 5, where energy and power density have been calculated with the active material mass in the anode and cathode. The maximum energy density of the cell is 100 Wh kg^{-1} (at 50 mA g^{-1}), and the maximum power density is 0.42 kWh kg^{-1} (at 1000 mA g^{-1}). The energy density of Sb–E1/NNMO full–cell is at par with rGO–Sb_2S_3/NNMO [41] (80 Wh kg^{-1}), Sb nanorod arrays/NNMO [42] (94.5 Wh kg^{-1}), and Sb-Ni nanorod arrays/NNMO [43] (100 Wh kg^{-1}) which all use NNMO cathode (all works calculate energy density with respect to active material mass in anode and cathode). The antimony–based anode reported in this work is synthesized through a scalable and easy process. The full–cell displayed a very high average working potential of ~2.9 V when cycled at a current density of 200 mA g^{-1}.

5. Conclusion

In summary, we have studied the electrochemical performance of antimony (III) oxide with exfoliated graphene oxide (EGO) as a volume buffer for the first time. The effect of EGO on the electrochemical performance of the half–cell was quantitatively evaluated, and Sb–E1 was seen to exhibit the best performance among the different materials. Sb–E1 displayed a higher initial discharge capacity of 545 mAh g^{-1} and good retention after 100 cycles at current density of 100 mA g^{-1}. The presence of EGO highly influenced the high current capacity and capacity retention after the high current testing. We determined that EGO provides cushioning during charge–discharge, promotes faster kinetics, and forestalls particle agglomeration. During the *in–situ* EIS study, the charge-transfer resistance (R_{CT}) was the highest during discharge, increasing from 0.40 V *vs.* Na and maximizing at 0.005 V *vs.* Na. The reverse trend was observed during charging, reaching a much lower value at 0.75 V *vs.* Na. These indicated that R_{CT} changes considerably during the alloying reaction of Sb^0 with Na^+. A full–cell was assembled with Sb–E1 anode and NNMO cathode, which exhibited promising results. The average operating potential was ~2.9 V, with a maximum energy density of 100 Wh kg^{-1} and a maximum power density of 0.42 kWh kg^{-1}. EGO is an excellent support for conversion–alloying–based materials that can circumvent the issues arising from the huge volume expansion during charge–discharge.

CRediT authorship contribution statement

Krishnan Subramanyan: Conceptualization, Investigation, Writing – original draft. **Murukabhavan Ramar Palmurukan:** Methodology, Investigation, Resources. **Yun-Sung Lee:** Resources, Writing – original draft, Funding acquisition. **Vanchiappan Aravindan:** Conceptualization, Writing – review & editing, Supervision, Funding acquisition.

Declaration of Competing Interest

The authors declare that they have no known competing financial interests or personal relationships that could have appeared to influence the work reported in this paper.

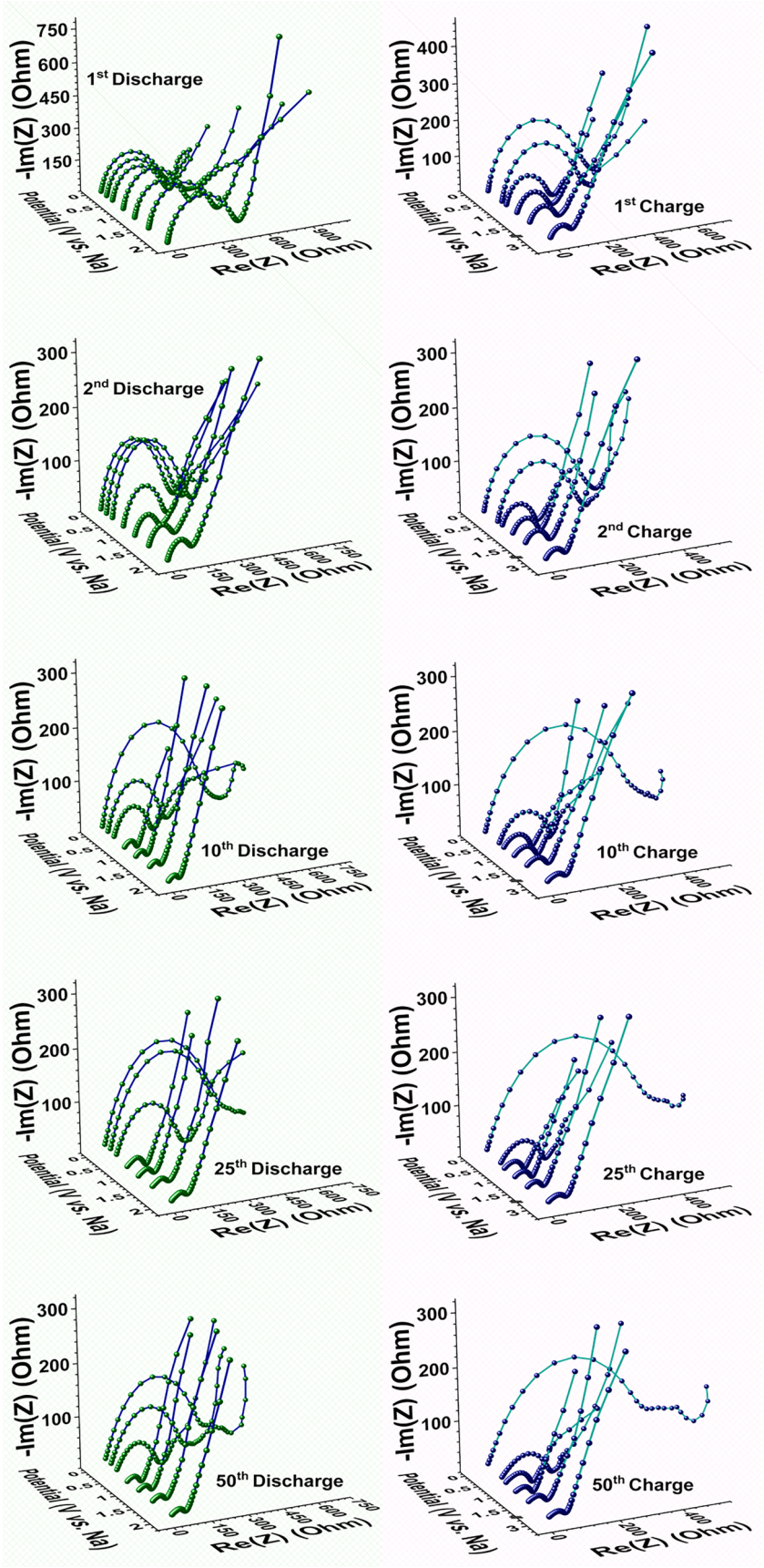

Fig. 3. *In–situ* EIS study of Sb–E1 half–cell.

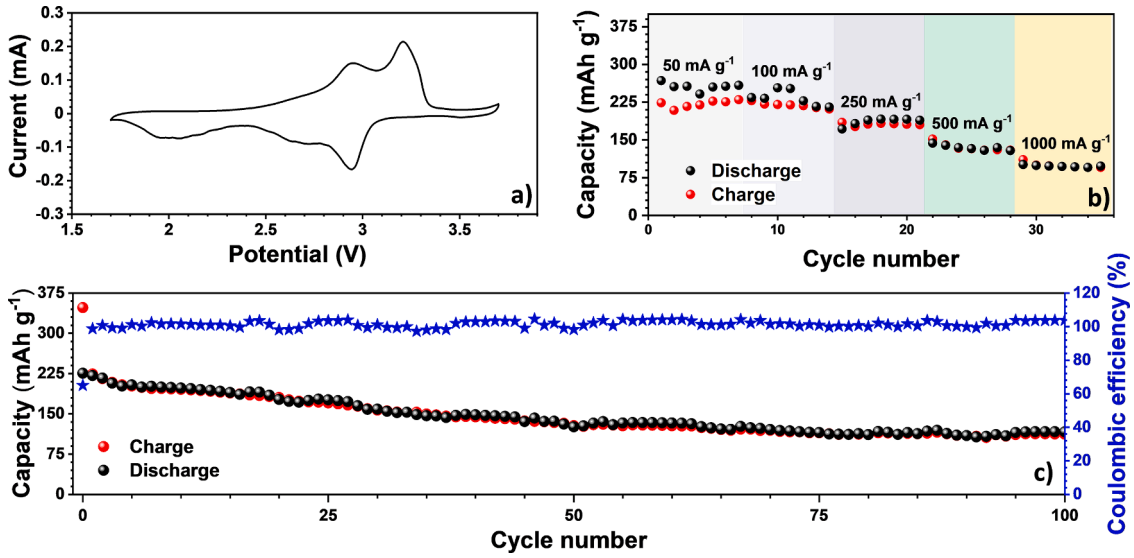

Fig. 4. **(a)** CV curve at a scan rate of 0.1 mV s^{-1}, **(b)** rate performance at current density of 50, 100, 250, 500, and 1000 mA g^{-1}, and (c) long–term cycling at current density of 200 mA g^{-1} (100 cycles) for Sb–E1/NNMO full–cell.

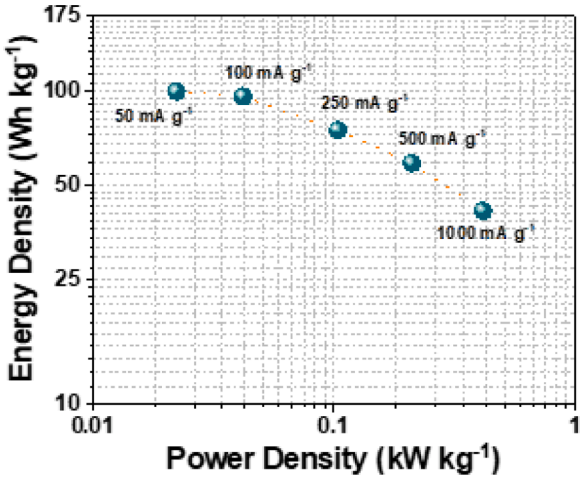

Fig. 5. Ragone plot of full–cell

Data availability

Data will be made available on request.

Acknowledgments

KS thanks the Department of Science & Technology (DST), Govt. of India, for the financial support through INSPIRE fellowship (IF180157). YSL acknowledges the financial support from the National Research Foundation of Korea (NRF) grant funded by the Korean government (Ministry of Science, ICT&Future Planning) (No. RS-2023-00208361). VA acknowledges financial support from the Science and Engineering Research Board, a statutory body of the DST, Govt. of India, through the Swarnajayanti Fellowship (SB/SJF/2020-21/12).

Supplementary materials

Supplementary material associated with this article can be found, in the online version, at doi:10.1016/j.electacta.2023.143308.

References

[1] R. Usiskin, Y. Lu, J. Popovic, M. Law, P. Balaya, Y.-S. Hu, J. Maier, Fundamentals, Status and Promise of Sodium-Based Batteries, Nat. Rev. Mater. 6 (11) (2021) 1020–1035.
[2] D. Karabelli, S. Singh, S. Kiemel, J. Koller, A. Konarov, F. Stubhan, R. Miehe, M. Weeber, Z. Bakenov, K.P. Birke, Sodium-Based Batteries: In Search of the Best Compromise Between Sustainability and Maximization of Electric Performance, Frontiers in Energy Research (2020).
[3] W. Zhang, F. Zhang, F. Ming, H.N. Alshareef, Sodium-Ion Battery Anodes: Status and Future Trends, EnergyChem 1 (2) (2019), 100012.
[4] H.S. Hirsh, Y. Li, D.H.S. Tan, M. Zhang, E. Zhao, Y.S. Meng, Sodium-Ion Batteries Paving the Way for Grid Energy Storage, Adv. Energy Mater. 10 (32) (2020) 1–8.
[5] J.-Y. Hwang, S.-T. Myung, Y.-K. Sun, Sodium-Ion Batteries: Present and Future, Chem. Soc. Rev. 46 (12) (2017) 3529–3614.
[6] J.M. Lee, G. Singh, W. Cha, S. Kim, J. Yi, S.-J. Hwang, A. Vinu, Recent Advances in Developing Hybrid Materials for Sodium-Ion Battery Anodes, ACS Energy Lett 5 (6) (2020) 1939–1966.
[7] T. Perveen, M. Siddiq, N. Shahzad, R. Ihsan, A. Ahmad, M.I. Shahzad, Prospects in Anode Materials for Sodium Ion Batteries - A Review, Renew. Sustain. Energy Rev. 119 (2020), 109549.
[8] K. Subramanyan, V. Aravindan, Towards Commercialization of Graphite as an Anode for Na-Ion Batteries: Evolution, Virtues, and Snags of Solvent Cointercalation, ACS Energy Lett. (2022) 436–446.
[9] H. Hou, X. Qiu, W. Wei, Y. Zhang, X. Ji, Carbon Anode Materials for Advanced Sodium-Ion Batteries, Adv. Energy Mater. 7 (24) (2017), 1602898.
[10] B. Xiao, T. Rojo, X. Li, Hard Carbon as Sodium-Ion Battery Anodes: Progress and Challenges, ChemSusChem 12 (1) (2019) 133–144.
[11] L. Li, Y. Zheng, S. Zhang, J. Yang, Z. Shao, Z. Guo, Recent Progress on Sodium Ion Batteries: Potential High-Performance Anodes, Energy Environ. Sci. 11 (9) (2018) 2310–2340.
[12] H. Kang, Y. Liu, K. Cao, Y. Zhao, L. Jiao, Y. Wang, H. Yuan, Update on Anode Materials for Na-Ion Batteries, J. Mater. Chem. A 3 (35) (2015) 17899–17913.
[13] W. Luo, F. Shen, C. Bommier, H. Zhu, X. Ji, L. Hu, Na-Ion Battery Anodes: Materials and Electrochemistry, Acc. Chem. Res. 49 (2) (2016) 231–240.
[14] M. Lao, Y. Zhang, W. Luo, Q. Yan, W. Sun, S.X. Dou, Alloy-Based Anode Materials toward Advanced Sodium-Ion Batteries, Adv. Mater. 29 (48) (2017) 1–23.
[15] S. Liang, Y.J. Cheng, J. Zhu, Y. Xia, P. Müller-Buschbaum, A Chronicle Review of Nonsilicon (Sn, Sb, Ge)-Based Lithium/Sodium-Ion Battery Alloying Anodes, Small Methods 4 (8) (2020), 2000218.
[16] Y. Kim, K.-H. Ha, S.M. Oh, K.T. Lee, High-Capacity Anode Materials for Sodium-Ion Batteries, Chem. – A Eur. J. 20 (38) (2014) 11980–11992.
[17] L. Wang, J. Świątowska, S. Dai, M. Cao, Z. Zhong, Y. Shen, M. Wang, Promises and Challenges of Alloy-Type and Conversion-Type Anode Materials for Sodium–Ion Batteries, Mater. Today Energy 11 (2019) 46–60.
[18] L. Fang, N. Bahlawane, W. Sun, H. Pan, B.Bin Xu, M. Yan, Y Jiang, Conversion-Alloying Anode Materials for Sodium Ion Batteries, Small 17 (37) (2021), 2101137.
[19] B. Xu, S. Qi, P. He, J. Ma, Antimony- and Bismuth-Based Chalcogenides for Sodium-Ion Batteries, Chem. – An Asian J. 14 (17) (2019) 2925–2937.
[20] W.T. Jing, C.C. Yang, Q. Jiang, Recent Progress on Metallic Sn- and Sb-Based Anodes for Sodium-Ion Batteries, J. Mater. Chem. A 8 (6) (2020) 2913–2933.
[21] X. Li, J. Ni, S.V. Savilov, L. Li, Materials Based on Antimony and Bismuth for Sodium Storage, Chem. - A Eur. J. 24 (52) (2018) 13719–13727.

[22] X. Wei, X. Wang, X. Tan, Q. An, L. Mai, Nanostructured Conversion-Type Negative Electrode Materials for Low-Cost and High-Performance Sodium-Ion Batteries, Adv. Funct. Mater. 28 (46) (2018), 1804458.
[23] H. Zhang, I. Hasa, S. Passerini, Beyond Insertion for Na-Ion Batteries: Nanostructured Alloying and Conversion Anode Materials, Adv. Energy Mater. 8 (17) (2018).
[24] S. Sarkar, S.C. Peter, An Overview on Sb-Based Intermetallics and Alloys for Sodium-Ion Batteries: Trends, Challenges and Future Prospects from Material Synthesis to Battery Performance, J. Mater. Chem. A 9 (9) (2021) 5164–5196.
[25] J. He, Y. Wei, T. Zhai, H. Li, Antimony-Based Materials as Promising Anodes for Rechargeable Lithium-Ion and Sodium-Ion Batteries, Mater. Chem. Front. (2018) 437–455.
[26] W. Luo, J. Ren, W. Feng, X. Chen, Y. Yan, N. Zahir, Engineering Nanostructured Antimony-Based Anode Materials for Sodium Ion Batteries, Coatings (2021) 1233.
[27] W. Brehm, J.R. Buchheim, P. Adelhelm, Reactive and Nonreactive Ball Milling of Tin-Antimony (Sn-Sb) Composites and Their Use as Electrodes for Sodium-Ion Batteries with Glyme Electrolyte, Energy Technol. 7 (10) (2019), 1900389.
[28] K. Subramanyan, V. Aravindan, Stibium: A Promising Electrode toward Building High-Performance Na-Ion Full-Cells, Chem 5 (12) (2019) 3096–3126.
[29] W. Wang, X. Zhu, Y. Zhang, Y. Liu, Q. Zhang, L. Fu, Structural Designs for Accommodating Volume Expansion in Sodium Ion Batteries, Chinese J. Chem. 36 (9) (2018) 866–874.
[30] B. Chen, M. Liang, Q. Wu, S. Zhu, N. Zhao, C. He, Recent Developments of Antimony-Based Anodes for Sodium- and Potassium-Ion Batteries, Trans. Tianjin Univ. 28 (1) (2022) 6–32.
[31] G. Jaiswal, V.G. Landge, D. Jagadeesan, E. Balaraman, Iron-Based Nanocatalyst for the Acceptorless Dehydrogenation Reactions, Nat. Commun. 8 (1) (2017) 2147.
[32] A.L.J. Pereira, L. Gracia, D. Santamaría-Pérez, R. Vilaplana, F.J. Manjón, D. Errandonea, M. Nalin, A. Beltrán, Structural and Vibrational Study of Cubic Sb_2O_3 under High Pressure, Phys. Rev. B 85 (17) (2012), 174108.
[33] S.D. Gardner, C.S.K. Singamsetty, G.L. Booth, G.-R. He, C.U. Pittman, Surface Characterization of Carbon Fibers Using Angle-Resolved XPS and ISS, Carbon N. Y. 33 (5) (1995) 587–595.
[34] S.O. Ganiyu, M.J.G. de Araújo, E.C.T. de Araújo Costa, J.E.L. Santos, E.V. dos Santos, C.A. Martínez-Huitle, S.B.C Pergher, Design of Highly Efficient Porous Carbon Foam Cathode for Electro-Fenton Degradation of Antimicrobial Sulfanilamide, Appl. Catal. B Environ. 283 (2021), 119652.
[35] J. Sun, G. Zheng, H.-W. Lee, N. Liu, H. Wang, H. Yao, W. Yang, Y. Cui, Formation of Stable Phosphorus–Carbon Bond for Enhanced Performance in Black Phosphorus Nanoparticle–Graphite Composite Battery Anodes, Nano Lett. 14 (8) (2014) 4573–4580.
[36] M. Klinger, More Features, More Tools, More CrysTBox, J. Appl. Crystallogr. 50 (4) (2017) 1226–1234.
[37] M. Hu, Y. Jiang, W. Sun, H. Wang, C. Jin, M. Yan, Reversible Conversion-Alloying of Sb_2O_3 as a High-Capacity, High-Rate, and Durable Anode for Sodium Ion Batteries, ACS Appl. Mater. Interfaces 6 (21) (2014) 19449–19455.
[38] X. Guo, X. Xie, S. Choi, Y. Zhao, H. Liu, C. Wang, S. Chang, G. Wang, Sb_2O_3/MXene ($Ti_3C_2T_x$) Hybrid Anode Materials with Enhanced Performance for Sodium-Ion Batteries, J. Mater. Chem. A 5 (24) (2017) 12445–12452.
[39] X. Zhou, Z. Dai, J. Bao, Y.-G. Guo, Wet Milled Synthesis of an Sb/MWCNT Nanocomposite for Improved Sodium Storage, J. Mater. Chem. A 1 (44) (2013) 13727–13731.
[40] Q. Liu, Z. Hu, M. Chen, C. Zou, H. Jin, S. Wang, Q. Gu, S. Chou, P2-Type $Na_{2/3}Ni_{1/3}Mn_{2/3}O_2$ as a Cathode Material with High-Rate and Long-Life for Sodium Ion Storage, J. Mater. Chem. A 7 (15) (2019) 9215–9221.
[41] E. Edison, S. Sreejith, S. Madhavi, Melt-Spun Fe-Sb Intermetallic Alloy Anode for Performance Enhanced Sodium-Ion Batteries, ACS Appl. Mater. Interfaces 9 (45) (2017) 39399–39406.
[42] L. Liang, Y. Xu, C. Wang, L. Wen, Y. Fang, Y. Mi, M. Zhou, H. Zhao, Y. Lei, Large-Scale Highly Ordered Sb Nanorod Array Anodes with High Capacity and Rate Capability for Sodium-Ion Batteries, Energy Environ. Sci. 8 (10) (2015) 2954–2962.
[43] L. Liang, Y. Xu, L. Wen, Y. Li, M. Zhou, C. Wang, H. Zhao, U. Kaiser, Y. Lei, Hierarchical Sb-Ni Nanoarrays as Robust Binder-Free Anodes for High-Performance Sodium-Ion Half and Full Cells, Nano Res. 10 (9) (2017) 3189–3201.